A bioprinted 3D gut model with crypt-villus structures to mimic the intestinal epithelial-stromal microenvironment

Núria Torras [a,*], Jon Zabalo [a,1,2], Eduardo Abril [a], Albane Carré [a,3], María García-Díaz [a,*], Elena Martínez [a,b,c,**]

[a] Biomimetic Systems for Cell Engineering Laboratory, Institute for Bioengineering of Catalonia (IBEC), The Barcelona Institute of Science and Technology (BIST), Baldiri Reixac 15-21, 08028 Barcelona, Spain
[b] Centro de Investigación Biomédica en Red (CIBER), Av. Monforte de Lemos 3-5, Pabellón 11, Planta 0, 28029 Madrid, Spain
[c] Department of Electronics and Biomedical Engineering, University of Barcelona (UB), Martí i Franquès 1, 08028 Barcelona, Spain

ARTICLE INFO

ABSTRACT

The intestine is a complex tissue with a characteristic three-dimensional (3D) crypt-villus architecture, which plays a key role in the intestinal function. This function is also regulated by the intestinal stroma that actively supports the intestinal epithelium, maintaining the homeostasis of the tissue. Efforts to account for the 3D complex structure of the intestinal tissue have been focused mainly in mimicking the epithelial barrier, while solutions to include the stromal compartment are scarce and unpractical to be used in routine experiments. Here we demonstrate that by employing an optimized bioink formulation and the suitable printing parameters it is possible to produce fibroblast-laden crypt-villus structures by means of digital light projection stereolithography (DLP-SLA). This process provides excellent cell viability, accurate spatial resolution, and high printing throughput, resulting in a robust biofabrication approach that yields functional gut mucosa tissues compatible with conventional testing techniques.

1. Introduction

In vivo, epithelial tissues are usually forming complex three-dimensional (3D) architectures that provide cells with specific microenvironments [1,2]. One of the most prominent examples is the small intestinal tissue, which folds forming finger-like protrusions called villi and invaginations called crypts. These microstructures are responsible for the exquisite cell type distribution along the crypt-villus axis of the tissue, the maintenance of cell renewal and homeostasis, the creation of oxygen gradients for the microbiome and maximizing absorption area and residence time for slow absorbing species [3–5]. Indeed, it is now well recognized that *in vitro* models of intestinal tissue accounting for its 3D architecture provide barrier properties (permeability and transepithelial electrical resistance, TEER) that better resemble *in vivo* values, thus improving the predictability of *in vitro* assays [6,7]. However, it is

also well known that the physiological function of the intestinal tissue does not only depend on a healthy epithelium, but also on the stromal tissue (named lamina propria) that lays below [2,8]. The entire structure, called intestinal mucosa, contains many cell types aside from the epithelial cells, including myofibroblasts, fibroblasts, endothelial cells and immune cells embedded in an extracellular matrix. These stromal cells have a key role in maintaining gut homeostasis and mucosal immunity [8,9]. Among them, mesenchymal cells secrete factors that are essential for the epithelial function and differentiation. It is therefore crucial to have access to intestinal tissue models that resemble not only the epithelium but the intestinal mucosa to properly model inflammatory bowel diseases, pathogen and microbiome interactions and cancer [10,11].

While in recent years there has been a lot of efforts to produce engineered tissues that recapitulate the architecture of the intestinal

tissue, in most of the cases those have been limited to represent only the epithelium. Mostly, this is due to the use of complex fabrication methods based on replica molding. These techniques require the use high macromer content materials (15–30 % *w/v* polymer content) with high stiffness rates (1 MPa to 2 GPa) to properly replicate the desired geometries [12], resulting in relatively high dense matrices that do not allow cell survival [13,14] or that are not friendly for embedding cells within [15,16]. Recently, some attempts have been made to include fibroblasts to mimic the stromal tissue in flat constructs [17], demonstrating the relevance of testing drug absorption in the presence of a full mucosa tissue. Also, there are some examples of including fibroblasts and other cell types in 3D structures employing replica molding, photolithography and laser ablation [9,18]. These techniques, however, rely on the use of expensive equipment, and/or time-consuming procedures, which ends with a limited throughput, as well as some restrictions in the type of materials used to ease the demolding. Therefore, the easy fabrication of cell friendly complex structures of high aspect ratio with soft materials (< 40 kPa) is still an open challenge [19].

Within this landscape, 3D bioprinting techniques offer unique features to tackle the problem. They offer a good resolution (compatible with most of the *in vivo* microstructures) and good fabrication speed, can be automatized, and are cost-effective [20,21]. Among bioprinting, extrusion-based and light-based approaches have been employed to produce models of gut tissues [14,22]. Extrusion-based devices are robust systems compatible with standard culture plates, in which bioinks are dispensed in drops or filaments through microscale print heat nozzles, requiring a postprocessing step for their stabilization [23,24]. Combinations of alginate, gelatin, type-I collagen and decellularized extracellular matrix (dECM) powder have been proposed as bioinks for the fabrication of 3D printed matrices resembling the characteristic villus-like structures of intestinal tissue; however, examples including the stromal compartment are still scarce [22,25]. The main drawbacks of extrusion-based bioprinting are the restrictions in bioinks' viscosity, the limited cell survival rates due to shear stresses inflected on cells during the printing process, and the low printing speed and printing resolution needed to preserve shape fidelity [26–28].

In parallel, light-based bioprinting techniques emerged as a strong alternative due to their easy access (several custom and commercially available models/alternatives), simplicity in use, versatility and low cost. In particular, digital light processing (DLP) 3D bioprinting based on stereolithographic (SLA) printing is gaining attention [29–31]. DLP-SLA photopolymerizes layer-by layer bioinks, which can include a suspension of cells. These bioinks are located inside a cuvette (or vat) that has a transparent window at the bottom and allows for the projection of focused white and black patterns to create the 3D printed elements. 3D structures including protruded features and cavities can be replicated from CAD-based designs with high fidelity and a precise control on the layer thickness, achieving in-plane *xy* resolution up to 25 μm [32,33]. Due to the high versatility of the technique and the affordability of the system components, several customized DLP-SLA bioprinters have been reported so far, working with a variety of bioinks such as gelatin, hyaluronic acid (HA), poly (vinyl alcohol) (PVA) and polyethylene glycol (PEG)-based polymers combined with photosensitive elements [32–34], and light -sources (typically in UV and visible range) [35–37].

Most of the light-based bioprinting approaches rely on free-radical polymerization using acrylate-based polymers. Since this polymerization reaction is typically difficult to confine for low content and transparent polymer solutions, efforts have derived in strategies to gain control on pattern definition. For instance, PEG-based polymers have been successfully mixed with photoabsorbing species to improve the spatial control of the polymerization [32,34]. However, when targeting cell embedding with these materials, they naturally lack cell-adhesion and degradation motifs, impairing cell spreading and proper functioning, and therefore limiting the cell survival rate. An alternative is the use of natural derived hydrogels such as gelatin methacryloil (GelMA), which can also be crosslinked using light. Despite its good properties,

when used at low concentrations, GelMA hydrogels are not mechanically stable, compromising the geometrical shape of the designs and lifespan of the printed constructs [38]. Previous works have highlighted the benefits of combining poly(ethylene glycol) diacrylate (PEGDA) and GelMA polymers for the biofabrication of cell-laden scaffolds for *in vitro* studies [13,39].

Here we present a customized DLP-SLA 3D bioprinting system for the direct printing of intestinal tissue constructs, including both the epithelial and stromal compartments, using transparent, soft hydrogels, by means of visible-light photopolymerization. The system has been adapted to work with reduced bioink volumes and environmental control, allowing the fabrication of cell-laden structures resembling the intestinal mucosa in a single printing step. With the proper tuning of (i) the GelMA-PEGDA bioink composition, (ii) the printing parameters such as layer thickness and exposure time, and (iii) the morphology of the CAD designs, we succeeded in the bioprinting of soft high aspect ratio hydrogels mimicking the intestinal mucosa, including villi and crypts with physiological dimensions and the epithelial and stromal compartments. Once printed, samples can be recovered with high fidelity and throughput, and allocated within standard Transwell® inserts, where can sustain long-term culture with high cellular viability. The encapsulated intestinal stromal cells supported the growth of the epithelial monolayer and adopted an *in vivo*-like distribution and morphology along the crypt-villus axis, whereas the epithelial cells showed a columnar morphology and the expression of polarization markers characteristic of differentiated enterocytes. Thus, we recreated the epithelial-stromal microenvironment in an intestinal mucosa 3D model using a simple DLP-bioprinting strategy, proving the suitability of the technique for the fabrication of improved and more reliable engineered tissue models for *in vitro* studies.

2. Materials and methods

2.1. Materials

Gelatin methacryloil (GelMA) was prepared following a method previously described [40,41]. Briefly, a 10 % (*w/v*) gelatin solution was first obtained by dissolving gelatin from porcine skin type A (Sigma-Aldrich) in phosphate buffer saline (PBS; pH 7.4) (Gibco) at 50 °C for 2 h under stirring conditions. Methacrylic anhydride (Sigma-Aldrich) at 1.25 % *v*/v was added at a rate of 0.5 mL/min and left to react for 1 h while stirring. The solution was centrifuged at 1200 rpm for 3 min and the reaction was stopped by adding Milli-Q water. The resulting solution was dialyzed using 6–8 kDa molecular weight cut-off membranes (Spectra/por, Spectrumlabs) against Milli-Q water at 40 °C, which was replaced every 4 h for 3 days. Then, after adjusting the pH to 7.4, the dialyzed products were frozen overnight at −80 °C and lyophilized for 4–5 days (Freeze Dryer Alpha 1–4 LD Christ). The resulting product, GelMA, with a methacrylation degree of 47.5 ± 4 % (determined by Trinitrobenzene sulfonate assay, data not shown) was stored at −20 °C until further use. A set of printing solutions (bioinks) was then prepared by mixing GelMA, poly(ethylene glycol) diacrylate (PEGDA) with a molecular weight of 4000 Da (Polysciences), visible-light lithium phenyl-2,4,6-trimethylbenzoylphosphinate (LAP) photoinitiator (TCI Europe), and tartrazine food dye (Acid Yellow 23, Sigma-Aldrich) at different *w/v* ratios and combinations using either Hank's Balanced Salt Solution (HBSS) (Sigma-Aldrich) or high glucose Dulbecco's Modified Eagle Medium (DMEM) without phenol red (Gibco) as dilution buffers.

2.2. DLP-SLA-based bioprinting platform

A customized digital light processing stereolithography (DLP-SLA) 3D bioprinting system was built by modifying a commercially available, low-cost Solus 3D printer (Junction3D), initially designed to print hard resins. As shown in Fig. 1A, the system consists of the following main components: a facing-down printing support coupled to a *Z*-axis motor, a
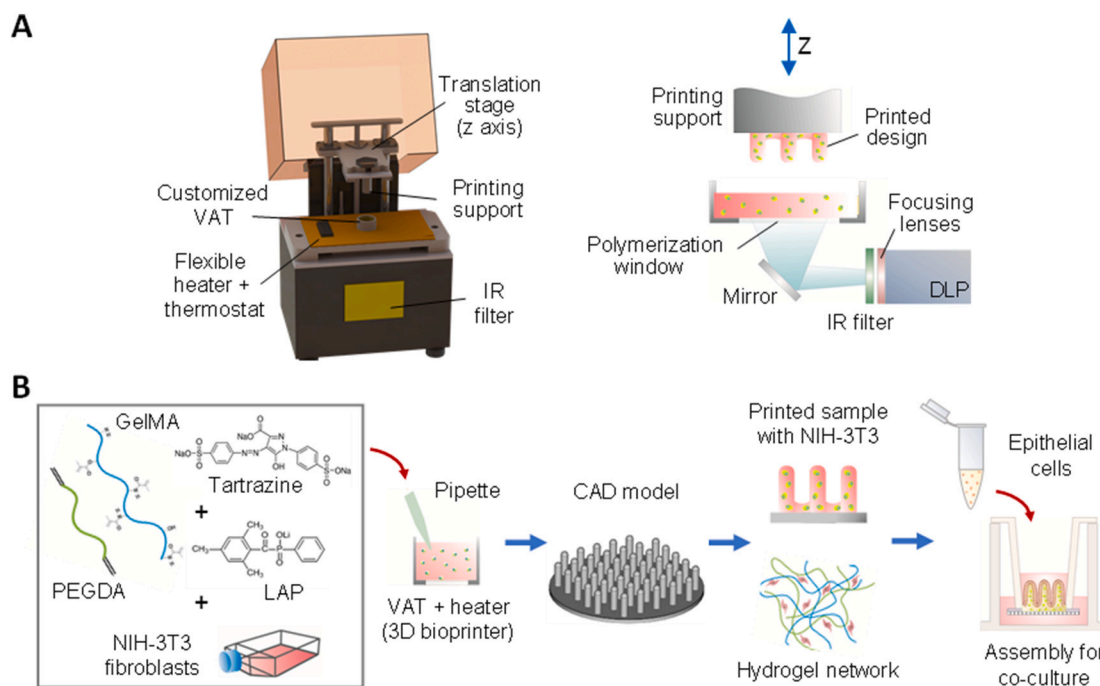
Fig. 1. Custom 3D bioprinting system: (A) 3D CAD model of our 3D bioprinter system (left) with detailed view of the main components (right). (B) Schematic illustration of the procedure followed for the fabrication of the proposed gut 3D model containing NIH-3 T3 fibroblast encapsulated in microstructured hydrogel co-networks (stromal compartment), co-cultured with Caco-2 epithelial cells.

resin vat with a transparent window, and a beam projector. A customized aluminum printing support and an aluminum vat were designed for printing small samples (between 3 and 10 mm in diameter) using reduced prepolymer volumes (< 2 mL). Aluminum was chosen for its good thermal conductivity and its low oxygen permeability. A high-definition FEP film (FEPshop) of 50 μm in thickness was used to create a flexible transparent window at the bottom of the vat to allow the pattern transfer to the prepolymer solution. This creates, at the same time, an oxygen permeable window to tune the free radical photo-polymerization reaction (Fig. S1). Additionally, a flexible heater with a thermostat (TUTCO) was coupled to the system to keep the prepolymer solutions warmed at 37 °C, preventing physical gelation, and allowing for the use of cell-laden polymers as bioinks. A full High-Definition 1080p resolution projector (Vivitek) was employed to crosslink the polymeric network using visible light. To avoid cell damage due to IR radiation exposure, a short pass heat protection filter (Schott) was added to the output of the projector. To form the 3D printed design, series of focused white and black patterns were projected onto the photo-crosslinkable prepolymer solution through the transparent vat window, forming the 3D structure in the vertical direction, layer by layer. The optical power density applied for printing was set between 3.1 and 12.3 mW/cm^2 (measured at the printing plane) through 5 predefined intensity levels in the projector (see Fig. S3) within the 320 to 640 nm wavelength spectral range. For the bioink compositions and the designs selected here, printing parameters were varied as following: layer thickness between 10 and 25 μm and exposure time per layer between 1 and 15 s.

2.3. Optimization of the bioprinting parameters

Printed designs in the shape of the crypt-villus architecture of the small intestinal tissue were tested with the customized DLP-SLA platform, using a bioink composed of 5 % *w/v* GelMA, 3 % w/v PEGDA and 0.4 % w/v LAP. To minimize undesired overexposure effects and have a finer control of the photocrosslinking process, the photoabsorber tartrazine was added to the mixture. All the components were dissolved in

HBSS supplemented with 1 % *v/v* Penicillin-Streptomycin (Sigma-Aldrich) at 65 °C under stirring conditions for 2 h or until properly dissolved. The final prepolymer solutions were kept at 37 °C for about 30 min before use. Then, the working prepolymer solution was pipetted into the vat of the DLP-SLA system, which was previously warmed at 37 °C. The CAD design was printed layer by layer from the bottom, on top of silanized 12 mm diameter glass coverslips or 10 mm diameter Tracketch® polyethylene terephthalate (PET) membranes with 5 μm pore size (Sabeu GmbH & Co) as printing support [6]. Once the printing process was finished, the hydrogels were rinsed in warmed PBS at 37 °C to remove unreacted polymer before being transferred to cell culture well plates and/or Transwell® inserts.

The influence of the relevant printing parameters (photoabsorber content, exposure time per printed layer and the printed layer thickness) on the bioprinting outcome was checked using CAD models, which include a disc-like base with an array of bullet-shape pillars, mimicking the intestinal villi. Each printing parameter was evaluated individually in a systematic manner, and the resulting prints were analyzed right just after fabrication to avoid possible distortions due to hydrogel swelling. Bright field pictures from top and lateral view were taken using a stereo microscope (Olympus, SZX2-ILLB) and processed with ImageJ software (http://imagej.nih.gov/ij, NIH) to obtain the printed dimensions of the different elements in the CAD models. The base thickness, the villus height and crypt diameter and depth were obtained from samples cross-sections, after cutting them with a blade.

2.4. Mechanical properties of the 3D printed hydrogels

To determine the bulk mechanical properties and flow characteristics of the printed hydrogels, rheological measurements were performed. First, disc-like samples of 8 mm in diameter and 0.5 mm in height were printed using the selected bioink formulation, 5 % *w/v* GelMA, 3 % w/v PEGDA, 0.4 % w/v LAP and 0.025 % w/v of tartrazine. As controls, prepolymer solutions containing, 8 % w/v PEGDA +0.4 % w/v LAP, and 8 % w/v GelMA +0.4 % w/v LAP both with the same tartrazine content were also included in these experiments. Samples

were allowed to reach equilibrium swelling by being submerged in HBSS at 4 °C for 5 days. As sample dimensions changed after swelling, they were punched to obtain 8 mm diameter samples for testing. Rheological tests were performed on a MCR302-PP08 rheometer (Anton Paar) equipped with parallel sandblasted plates of 8 mm in diameter. Measurements were performed using a sinusoidal signal and applying a sweep to the amplitude of shear strain between 0.01 % and 500 % while keeping constant the angular frequency to 10^{-1} s. The running temperature was maintained at 23 °C throughout the measurements. Values of both storage (G') and loss (G'') moduli were obtained as a function of the strain, from which the elastic component of the moduli, E, was derived assuming a value for the Poisson's ratio of 0.5.

2.5. Diffusivity properties of the 3D printed hydrogels

A diffusion study was performed to experimentally estimate the mesh size of the printed hydrogels, since other methods, such as the one based on the Flory-Rehner theory, are not applicable when working with hydrogel co-networks [42]. To do so, the diffusion profiles of dextran fluorescent molecules of different molecular weights passing through the hydrogels were analyzed. Disc-like samples of 6.5 mm in diameter and 0.5 mm in height were printed using prepolymer solution containing 5 % *w/v* GelMA, 3 % w/v PEGDA, 0.4 % w/v LAP and 0.025 % w/v of tartrazine in HBSS supplemented with 1 % *v/v* Penicillin-Streptomycin. After printing, hydrogels were mounted on Transwell® inserts using double-sided pressure sensitive adhesive (PSA) rings (Adhesive research) and left in standard cell culture conditions (37 °C and 5 % CO_2) to reach equilibrium swelling. Dextran molecules of 4 kDa (FITC-Dextran), 70 kDa (Rhodamine- Dextran), 150 kDa (FITC-Dextran), 500 kDa (FITC-Dextran) and 2000 kDa (FITC-Dextran) (all from Sigma-Aldrich) were used separately at a concentration of 0.5 mg/mL in PBS. Then, 200 μL of the pre-warmed dextran solutions were loaded in the apical compartment while adding 600 μL of PBS to the basolateral chamber. The plates were then incubated at 37 °C and at regular time intervals, 50 μL were withdrawn from the basolateral compartments and replaced with warmed PBS. Collected samples were transferred to black 96-well plates and the FITC or Rhodamine fluorescence was measured using an Infinite M200 PRO Multimode microplate reader (Tecan), at excitation/emission wavelengths of 490/525 nm and 540/625 nm, respectively. The changing concentration of dextrans over time was determined using standard calibration curves and the diffusion coefficients (D) were calculated following the method form [43,44].

$$-\ln\left(1 - \frac{C(t)}{N/V}\right) = \frac{D}{h}\left(\frac{t}{\tau}\right)$$

$$V = V_{apical} + Ah + V_{basolateral}$$

$$\tau = \frac{\left(V_{apical} + \frac{Ah}{2}\right)\left(V_{basolateral} + \frac{Ah}{2}\right)}{AV}$$

where $C(t)$ is the dextran concentration in the basolateral chamber over time t, N is the total dextran mass, h is the height of the hydrogels, V is the total volume and A is the area in which the diffusion occurs.

2.6. Cell culture conditions

NIH-3T3 fibroblasts (ATCC® CRL-1658™) from passages 12 to 17 were used for printing cell-laden hydrogels to mimic the cell population within the stromal compartment of the intestinal mucosa. Fibroblasts were grown, expanded, and maintained at 37 °C and 5 % CO_2 in 175 cm^2 culture flasks using high glucose DMEM (Gibco, ThermoFisher), supplemented with 10 % *v/v* fetal bovine serum (FBS) (Gibco, ThermoFisher) and 1 % v/v Penicillin-Streptomycin (Sigma-Aldrich). Cells were passaged twice a week, exchanging the medium every other day. Caco-2

cells (ATCC® HTB-37TM) from passages 83 to 87 were seeded on top of the printed hydrogels (with and without embedded cells) to mimic the epithelial layer of the small intestine. Caco-2 were grown, expanded, and maintained in 75 cm^2 culture flasks in high glucose DMEM (Gibco, ThermoFisher), supplemented with 10 % v/v fetal bovine serum (FBS) (Gibco, ThermoFisher), 1 % v/v Penicillin/Streptomycin (Sigma-Aldrich) and 1 % v/v of non-essential amino acids (NEA) (Gibco, ThermoFisher). Cells were maintained at 37 °C and 5 % CO_2, changing medium every other day and passaged weekly.

2.7. Fabrication and characterization of cell-laden hydrogels with crypt-villus structures: mimicking the small intestinal tissue

Cell-laden hydrogels with the villous morphology of the small intestinal tissue were bioprinted to mimic the stromal compartment of the intestinal mucosa. NIH-3 T3 fibroblasts were trypsinised from the cell culture flasks and re-suspended in the prepolymer solutions to get bioinks with a cell density of $7.5·10^6$ cells/mL. Then, bioinks were immediately placed in the vat previously warmed at 37 °C and the printing process started. To maintain the cell suspension homogeneously distributed through the vat volume along the printing time, the prepolymer solution was stirred by gently pipetting. Samples were fabricated on silanized PET membranes by using a printing optical power density of 12.3 mW/cm^2. After the printing process, samples were washed out with warm cell culture medium supplemented with 1 % of Penicillin-Streptomycin to remove the unreacted polymer. Then, the bioprinted cell-laden hydrogels were attached to Transwell® inserts by PSA rings. Finally, Caco-2 cells were seeded on top of the samples at a density of $2.5·10^5$ cells/cm2 to mimic the intestinal epithelial layer. The samples were cultured for 21 days in an incubator at 37 °C and 5 % CO_2, replacing medium every other day.

2.8. Viability of cells embedded onto the 3D printed hydrogels

Fibroblast viability within the bioprinted cell-laden hydrogels was investigated employing a calcein-AM/ethidium homodimer Live/Dead kit (Invitrogen), 24 h, 7 and 10 days after NIH-3 T3 cell encapsulation. Hoechst was used as live staining for the nuclei. A confocal laser scanning microscope (LSM 800, Zeiss) was used for imaging and a manual cell counter plugin in ImageJ software (http://imagej.nih.gov/ij, NIH) was employed for image processing and cell viability quantification.

2.9. Histological and immunofluorescence analysis

After 21 days in culture, the morphology and phenotype of both Caco-2 and NIH-3 T3 cells present in the bioprinted hydrogels featuring the intestinal crypt-villus microstructure were studied by immunostaining. Histological cuts were performed for this purpose. To preserve the morphology of the villus and crypt-like features on the soft hydrogels, samples were embedded following a protocol developed by our group [45]. Briefly, after fixation with 10 % neutral buffered formalin solution (Sigma-Aldrich) at 4 °C for 1 h, samples were submerged in a prepolymer solution containing 10 % *w/v* of PEGDA 575 kDa (Sigma-Aldrich) and 1 % w/v of 2-Hydroxy-4'-(2-hydroxyethoxy)-2-methylpropiophenone (Irgacure D-2959) photoinitiator (Sigma-Aldrich) in phosphate buffered saline (PBS) (ThermoFisher) and kept overnight at 4 °C. Then, samples were placed within poly(dimethyl siloxane) (PDMS) (Dow corning) round pools of 12 mm in diameter and 2 mm in thickness attached to a plastic support, which was filled with PEGDA 575 kDa prepolymer solution. The construct was then irradiated using UV light at 365 nm wavelength in a MJBA mask aligner (SUSS MicroTech). To ensure the formation of a homogeneous block, samples were irradiated twice for 100 s at 25 mW/cm^2 of power density, first from the top and then from the bottom, by flipping the sample downwards. An additional first exposure of 40 s was required to form a support base to keep the plastic support in place. After UV exposure, unreacted polymer and

photoinitiator were washed out with PBS. Then, samples on PEGDA blocks were immersed overnight in 30 % sucrose solution (Sigma-Aldrich) at 4 °C for cryoprotection, further embedded in OCT (Tissue-Tek® O.C.T. Compound, Sakura® Finetek) and stored at −80 °C for at least 12 h. Finally, they were cut with a cryostat (Leica CM195) and histological cross-sections sections of ~7 μm thickness were recovered, attached onto glass coverslips, air dried and stored at −80 °C until use.

For immunostaining, samples on glass coverslips were left to unfreeze overnight at room temperature (RT) and washed carefully with PBS. Then, cells were permeabilized with 0.5 % Triton-X (Sigma-Aldrich) at 4 °C for 2 h and blocked with 1 % bovine serum albumin (Sigma-Aldrich), 3 % donkey serum (Millipore), and 0.3 % Triton-X at 4 °C for 2 h. Drops of 50 μL containing primary antibodies against β-catenin (Abcam) (1 μg/mL), Ecadherin (BD Biosciences) (2.5 μg/mL), collagen IV (Biorad) (1.6 μg/mL), fibronectin (Santa Cruz) (2 μg/mL) and Laminin (Abcam) (0.65 μg/mL) were placed on top of the sections and incubated overnight in a moisture chamber at 4 °C under shaking conditions, and covered with Parafilm® (Sigma-Aldrich) to prevent drying. After several washing steps with PBS, samples were incubated with the secondary antibodies anti-goat Alexa 647, and anti-rabbit Alexa 488 or anti-mouse Alexa 488 (Invitrogen, ThermoFisher) (4 μg/mL) together with Rhodamine-Phalloidin (Cytoskeleton) (0.07 μM) for 2 h at 4 °C, and finally, were incubated with DAPI (5 μg/mL) for 30 min. In the case of anti ZO-1 staining (ThermoFisher) (2.5 μg/mL), an antigen retrieval treatment was performed prior sample permeabilization to enhance its signal. Briefly, samples were boiled for 10 min after unfreezing in citrate buffer solution (10 mM citrate and 0.05 % *v*/v of Tween20 in MilliQ water, previously adjusting the pH at 6), controlling bubble formation. Then, the staining procedure continued as for the other markers. After immunostaining, samples were covered by thin glass coverslips with a drop of Fluoromount G (Southern Biotech) and were imaged using a confocal laser-scanning microscope (LSM 800, Zeiss).

Some samples were also used for hematoxylin and eosin (H&E) staining. Briefly, once at RT, samples were incubated with Harris Hematoxylin (Sigma-Aldrich) for 2.5 min, with acid alcohol for 1 min, with ammonia water for 2 min and with Eosin solution (Sigma-Aldrich) for 1 min. Between each incubation, samples were rinsed in running cold water for 3 min. Finally, samples were dehydrated in increasing concentration of alcohols, cleared two times in xylene (Sigma-Aldrich), mounted in xylene-based mounting medium (Eukitt, Panreac) and imaged using transmitted light.

2.10. Epithelial barrier integrity measurements by monitoring the transepithelial electrical resistance (TEER)

The growth and integrity of the epithelial barrier formed on top of the 3D bioprinted hydrogels was assessed by monitoring the transepithelial electrical resistance (TEER) between the apical and basolateral compartments defined by the Transwell® inserts. This was tracked three times per week using an EVOM2 Epithelial voltohmmeter with an STX3 electrode (World precision Instruments) for a total culture time of 21 days. The resistance values measured were corrected by subtracting the resistance of the porous PET membranes of the Transwell® inserts and the resistance of the cell-free and cell-laden crypt-villus hydrogels. TEER values were normalized by the total surface area of the epithelial monolayers, taking into account the morphology of the printed features [6].

2.11. Statistics and data analysis

Graphpad Prism 8 software was used for data treatment and analysis. The data in graphs are presented as mean values with standard deviation (SD). In the case of normal distributions, statistical significance was interrogated by means of one-way ANOVA test. Turkey's test was also performed when indicated in the figure captions. Values of $p < 0.05$

were used to consider differences as statistically significant.

3. Results

3.1. Optimization of a low-cost DLP-SLA 3D printer allows the bioprinting of high-resolution soft hydrogel 3D constructs of low polymer content

To successfully employ our low cost DLP-SLA 3D printing system as bioprinter, we customized the device including (i) an aluminum-based dedicated printing support and vat suitable for small solution volumes (<2 mL), (ii) a flexible heater with a thermostat to keep the bioink solutions at 37 °C allowing for the use of cell-laden polymers, and (iii) an infrared (IR) filter coupled to the output of the projector to minimize cell damage (Fig. 1A). As bioink we used a GelMA-PEGDA prepolymer solution containing 5 % *w/v* GelMA and 3 % w/v PEGDA, using 0.4 % w/v LAP as photoinitiator (Fig. 1B). The low concentration of high molecular weight polymers was chosen to favor the spreading and migration of the embedded cells; however it challenged the printability of the high aspect-ratio villus-like structures. Previous works used bioinks with higher macromer content polymers (typically ranging from 10 to 30 % (*w/v*)) to guarantee self-standing features maintaining the printing resolution [29,34], resulting in dense matrices not suitable for bioprinting purposes. In this work, we aimed at optimizing the printing parameters to obtain robust high-aspect ratio structures with low polymer content to allow for cell embedding. To improve the resolution of our printing results, an additional photoabsorbing agent (tartrazine) was added to the bioink mixture. This synthetic azo dye highly soluble in water has an absorption peak centered around 436 nm, overlapping both the emission spectrum of our light source, and the LAP absorption peak (~375 nm), resulting in a beneficial mixture for printing well defined 3D structures [46]. NIH-3 T3 mouse embryonic fibroblasts were chosen to validate the suitability of our setup for bioprinting, since they are commonly used for cell encapsulation experiments [13,47]. In addition, these cells represent the fibroblast cell population within the stromal compartment of our intestinal model. Indeed, this cell type has been extensively used in co-cultures with murine but also with human cells as feeder layer [48], and has been reported to enhance epithelial proliferation and differentiation *via* paracrine effects when co-cultured with Caco-2 epithelial cells [47,49]. For this purpose, 7.5·10^6 cells/mL were mixed with the GelMA-PEGDA bioink. The mixture was placed in the vat and the CAD design model with the optimized intestinal villous structures (see Supplementary Information and Fig. S4) was printed. Cell-laden samples were printed on top of treated porous PET membranes to be later mounted on Transwell® inserts for cell culture (Fig. 1B).

In order to mimic the small intestine architecture, different CAD models including both extruded features resembling the villi and holes recreating the crypts of the tissue were produced and printed. Crypts and villus heights, diameters, and distances among them (*i.e.*, pitch) were varied according to reported values for this tissue in humans (Fig. S4) [50]. A hydrogel base in the shape of a thin disc was added as handling support for the whole structure as well as for the cells to feel the mechanical properties of the soft material. The optimized CAD design was selected with a base thickness of 250 μm, invaginations of 150 μm, and protrusions of 700 μm (Fig. 2A), leading to homogeneous, well-defined self-standing crypt-villus features with physiologically relevant dimensions (Fig. 2B). In DLP-SLA systems, the total printing time (also known as building time) is dependent on the predefined layer thickness and the single layer exposure time [31]. So, in terms of throughput, large layer thicknesses and short exposure times should be beneficial. Moreover, since we used a bioink with a low polymer content, the printing parameters should be carefully optimized. Thus, we evaluated the effect of the concentration of the photoabsorbing agent, single layer exposure time and layer thickness on the morphology of the bioprinted intestinal mucosa constructs (Fig. 2C). As stated before, we used tartrazine as a photoabsorber to better confine the photopolymerization reaction. Fixing the printing parameters to 61.5 mJ/cm^2 as exposure energy dose
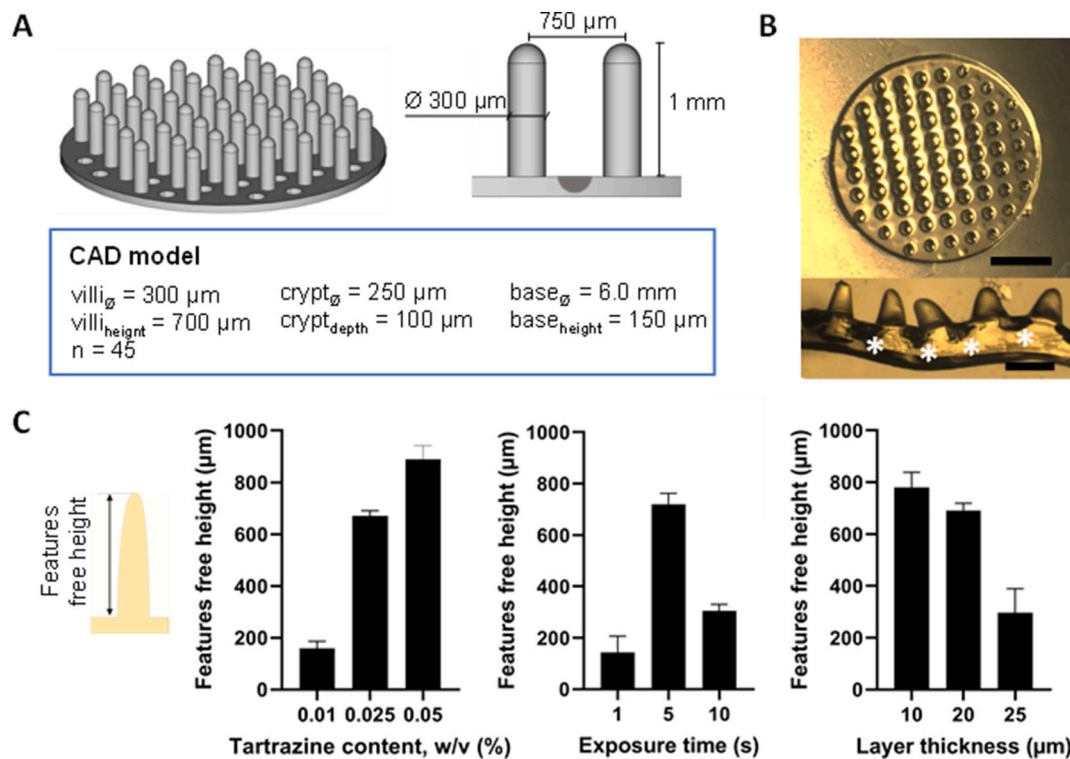
Fig. 2. Impact of the printing parameters on the 3D microstructures. A) CAD design with the optimized villus and crypt dimensions for the fabrication of the final prints (B), corresponding printing results obtained using 5 % w/v GeLMA, 3 % w/v PEGDA, 0.4 % w/v LAP and 0.025 % *v*/v tartrazine as bioink. Scale bar = 1.5 mm (top views), 400 μm (cross-section).

per layer, with a predefined layer thickness of 13 μm (net *z* motor displacement), we tested three different GelMA-PEGDA-LAP bioinks with tartrazine at concentrations of 0.01, 0.025 and 0.05 % *w*/v (0.19, 0.47 and 0.94 mM, respectively), which are below the cytotoxic range of this dye (2.5–4 mM) [51,52]. As observed in Fig. S5A, for the lowest tartrazine concentration, the crosslinking confinement was not efficient and it was extended to the regions with no direct light exposure, resulting in overexposed structures. As a consequence, 3D microstructures looked as partially embedded within a thick base, significantly decreasing their free height (tip to base distance) of about 80 % compared to the intended dimensions (Fig. 2C, left pannel). When increasing the tartrazine concentration to 0.025 % *w*/v the crosslinking reaction was better confined, and significantly thinner and larger features were obtained. For the highest tartrazine concentration tested (0.05 % *w*/v), the crosslinking was confined very efficiently, and the features were well defined but, for the high aspect ratio of the 3D microstructures structures did not self-stand (Fig. S5A).

Thus, the optimized GelMA-PEGDA-LAP bioink with tartrazine at a concentration of 0.025 % w/v was used to evaluate the effects of two printing parameters on the morphology of the 3D microstructured hydrogel: the exposure time and layer thickness. We first varied the single layer exposure time between 1 and 10 s, applying an incident optical power of 12.3 mW/cm^2 and a fixed thickness per printed layer of 18 μm. A poorly crosslinked hydrogel was obtained for the lowest exposure time tested (Fig. S5B), probably because the energy dose applied per printed layer *E* (12.3 mJ/cm^2) was lower to the estimated critical energy needed for the polymer chains to achieve enough crosslinking degree and form a gel, E_c (~35 mJ/cm^2) for our particular approach. Increasing the exposure time up to 5 s, we obtained well crosslinked finger-like 3D microstructures of a free height matching the one defined by the CAD design and with the proper aspect ratio (Fig. 2C). Longer exposure times allowed the propagation of the crosslinking reaction to regions not illuminated by the pattern, triggering an overexposure reaction. The evaluation of the impact of the layer

thickness on the morphology of the 3D microstructured scaffolds was performed by fixing the exposure energy to 61.5 mJ/cm^2 (*i.e.* 5 s of single exposure time), varying the layer thickness between 10 and 25 μm. As shown in Fig. S5C, the smallest thickness values tested per printed layer resulted in self-standing 3D microsctructured features, with some overexposure localized at the surrounding regions, but nice free feature heights close to those imposed by the CAD design (Fig. 2C). Thicker layer thicknesses, however, resulted in less defined features that did not self-stand (Fig. S5C). These results are in agreement with previous findings above and proved that, for a given bioink composition and energy dosage, lower voxel units (*i.e.* shorter layer thicknesses) can be achieved, enhancing the printing resolution [32].

3.2. Mechanical and diffusion properties of bioprinted GelMA-PEGDA hydrogels of optimized composition

The network architecture of hydrogels is directly correlated with their water uptake capacity, which affects the penetration and transport of essential nutrients and oxygen [53]. Hence, it is relevant to characterize the swelling properties of the hydrogels produced using the predefined bioink formulation and printing parameters leading to the optimized crypt-villus scaffolds (see supplementary information and Fig. S6). The swelling ratio measured for our 3D bioprinted hydrogels was significantly lower than previous values reported for GelMA-PEGDA co-networks of similar macromer content (3.75 % *w*/v GelMA - 3.75 % w/v PEGDA) but different polymer rate [13]. It is recognized that GelMA-PEGDA hydrogels exhibit tailorable swelling properties, which primary depend on the GelMA's methacrylation degree and the total macromer concentration. PEGDA is a hydrophilic polymer whose molecules have two binding sides at the end of the chain, whereas GelMA has multiple crosslinking points over the chain, in agreement with its methacrylation degree. Thus, increasing the GelMA content of our bioink, denser networks can be achieved, leading to lower swelling rates due to its decreased interaction with water molecules [53].

Furthermore, the printing parameters chosen, such as the energy dose applied, and the nature and concentration of the photoinitiator used, have also been proved to have a direct impact on the swelling behavior of the bioink [54]. Additionally, in this case, the presence of a photo-absorbing agent in the bioink composition affects the photo-polymerization process (Fig. 2C and Fig. S5A), also altering the swelling properties.

Another parameter that is of paramount importance when embedding cells in a 3D matrix is the stiffness of such matrix, which ideally should be close to the *in vivo* tissue. For the intestinal tissue, elastic moduli values ranging from 1 to 100 kPa are reported [55,56]. Fig. 3A shows the components of the complex shear modulus measured as a function of the shear strain. The plots revealed a typical behavior characteristic of viscoelastic solids ($G' > G''$) with a certain degree of crosslinking in its network structure [57]. We also determined that, as previously observed in the printing results and the swelling behavior, the crosslinking degree and thus, the mechanical properties, can be tuned by just changing the tartrazine concentration (Fig. S7). For the optimized bioink solution, which included tartrazine at a concentration of 0.025 % *w/v*, the storage modulus G' measured from the linear region of the curve (up to 0.01 % of the shear stress) was 2.07 ± 0.41 kPa. This value lays between those obtained for 8 % w/v GelMA and 8 % w/v PEGDA, being closer to the latest (Fig. 3B). Considering our hydrogels as quasi-isotropic materials (Poisson's coefficient of ~0.5), the apparent elastic moduli when adding 0.025 % *w/v* of tartrazine to the bioink composition resulted in 5.94 ± 0.19 kPa, evidencing the softness of our gels. Moreover, these values obtained in agreement with others reported in literature for PEGDA- and GelMA-based hydrogels [6,58,59], as well as with the ones from other materials typically employed for *in vitro* 3D tissue cultures, such as Matrigel® and Collagen I, measured using similar standard assays [60]. In addition, the mechanical properties measured for our bioprinted hydrogels were within the range of the ones described for *in vivo* soft tissues [55].

3D matrices for cell cultures should also guarantee the transfer of nutrients and oxygen and the excretion of waste metabolites. These mass transfer properties are related with the porous structure of the bio-printed GelMA-PEGDA hydrogels. To gain insight on that, the diffusion profiles of model dextran compounds of different molecular sizes were measured, and their apparent diffusion coefficients through the hydro-gel co-network were estimated (Fig. 3C). While the hydrogel acted as a diffusion barrier for large molecules (500 and 2000 kDa, see Fig. S8), it allowed the diffusion of small (4 kDa) and medium size molecules (70 and 150 kDa). The size exclusion limit, defined as the smallest dextran diameter excluded from the pores, was determined from the plot of the diffusion coefficients *versus* the ln (MW) (see Fig. S4) [43]. The molecular weight exclusion limit was found to be 360 kDa (215 to 750 kDa, 95 % CI). This pore size ensures good mass transfer properties for the cell survival within the hydrogels since it allows for diffusion of molecules such as albumin (58 kDa), one of the most abundant proteins present in cell culture media.

3.3. Bioprinted GelMA-PEGDA hydrogels sustain cell culture effectively

Once the printing system and the model geometries were optimized and the hydrogel scaffolds characterized, NIH-3T3 fibroblasts as representatives for the intestinal stromal compartment were added to the prepolymer mixture. First, the distribution of fibroblasts within the intestinal bioprinted samples was investigated *via* H&E and F-actin staining at different culture time points using both histological cuts and full thickness samples. At different time points after encapsulation, samples were fixed and embedded in low molecular weight PEGDA to protect the integrity of the soft 3D bioprinted microstructures, following the dedicated protocol developed by our group [45]. Thereafter, samples were embedded in OCT® medium and cross-sectioned before staining and imaging. 3 days after encapsulation, cells appeared homogeneously distributed within the whole volume of the hydrogel
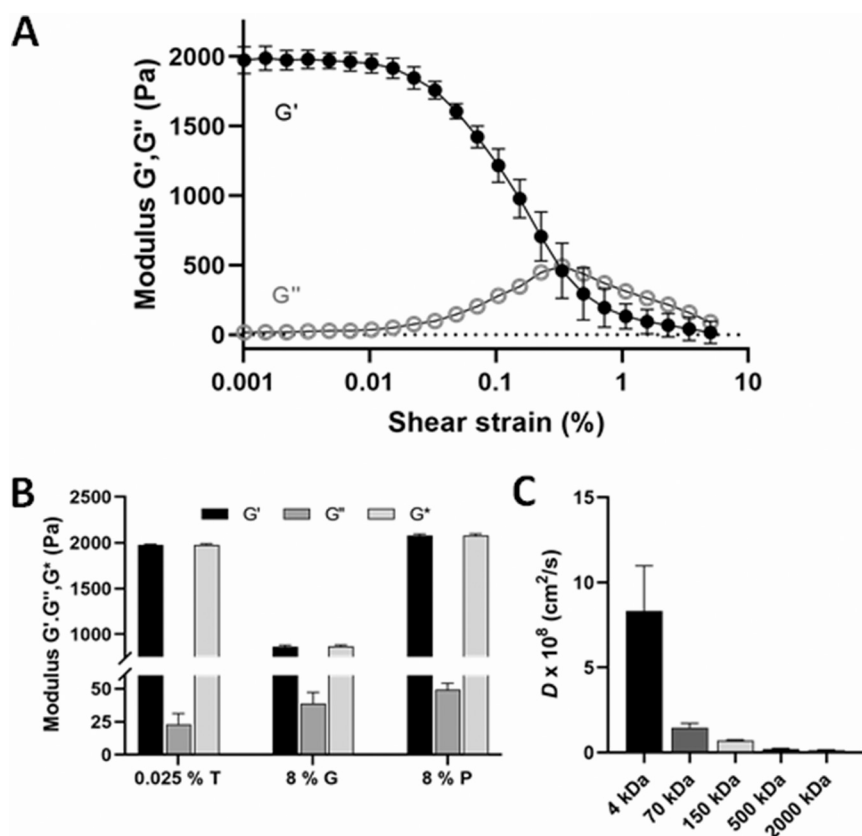
Fig. 3. Mechanical and diffusive properties of the bioprinted hydrogels: A-B) Mechanical performance of the printed gels for samples containing 0.025 % *w/v* of photo-absorber. Rheological curves showing G' and G'' moduli (A) and comparison of complex, storage and loss moduli (B). (C) Diffusion coefficients for dextran molecules of different sizes diffusing through the bioprinted hydrogels (FD2000 = 2000 kDa, with a hydrodynamic diameter of 41.6 nm; FD500 = 500 kDa, with a hydrodynamic diameter of 32 nm; FD150 = 150 kDa, with a hydrodynamic diameter of 17 nm; FD70 = 70 kDa, hydrodynamic diameter of 11.6 nm; FD4 = 4 kDa, hydrodynamic diameter of 2.8 nm). Results are shown as mean ± SD (min *n* = 3).
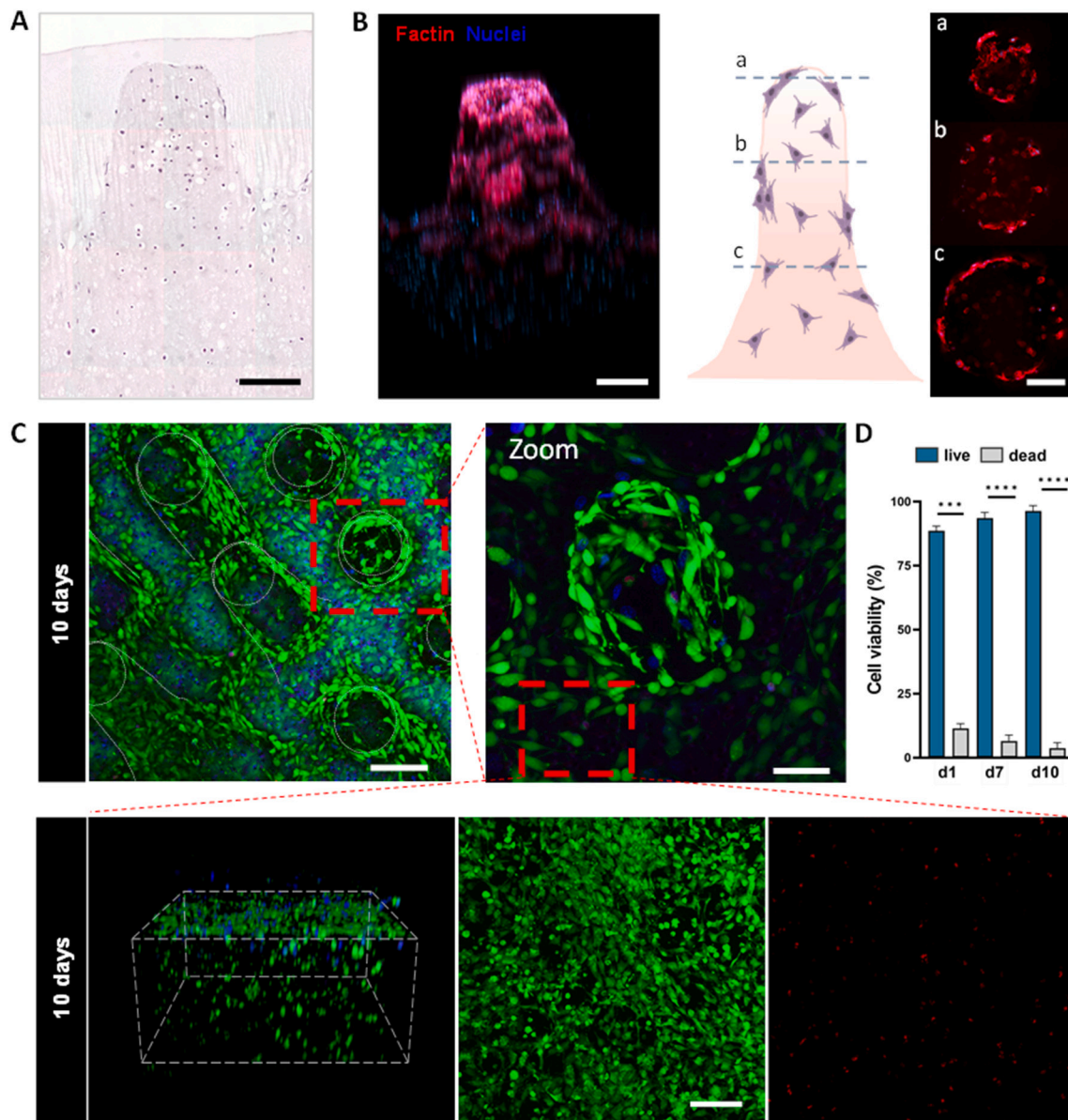
Fig. 4. Cell distribution and viability after bioprinting: (A-B) NIH-3 T3 distribution in 3D bioprinted cell-laden microstructures 3 days post encapsulation by means of H&E staining of histological cuts (A) and immunofluorescence of full thickness samples (B). F-actin (red) and nuclei (blue) show uniform fibroblasts distribution along and within the structure, evidenced by the transversal cuts (left). Cells near the surface appeared spread and elongated, whereas the ones inside the villi are still protruding. Scale bars = 50 μm. (C) Top maximum intensity projection of 3D bioprinted intestinal model 10 days post encapsulation after live/dead assay (live cells stain in green, dead cells in red), with detailed views of a single villi (right) and a single crypt region (bottom). Hoechst was used to stain the nuclei. Scale bars = 100 μm (top and 3D view) and 200 μm (zoom in regions). (D) Cell viability quantification based on live/dead staining, 1, 7 and 10 days post-encapsulation. Values are the mean percentage of cell viability +/− SD ($n = 4$). **** $p < 0.0001$; *** $p = 0.008$.

(Fig. 4A); being the ones closer to the surface and crypt regions starting to spread (Fig. 4B).

Cell viability within the bioprinted hydrogels was evaluated using a Calcein-AM/ethidium homodimer live/dead assay and confocal microscopy 1, 7, and 10 days after cell encapsulation. Fig. 4C shows the cells distribution in the printed samples 10 days post-encapsulation. Cells were well distributed within the hydrogels colonizing the 3D villous microstructures and forming an entangled mesh. Detailed views of a single villi tip and a crypt confirm these results (Fig. 4C, detailed views). Overall, the cell viability after the bioprinting process was excellent with this method (above 90 ± 2 %, 24 h post-encapsulation) (Fig. 4D). This might be related to a friendly bioprinting process and to the relatively small swelling of the bioinks we used, which minimizes cell stress after printing [13]. After 7 and 10 days in culture, the cell viability slightly

increased with respect to the values obtained 24 h after encapsulation, resulting in 93 ± 2 % and 96 ± 2 %, respectively. These results proved that both the bioink composition selected and the printing parameters, result in hydrogels able to sustain cell culture in an effective manner.

3.4. Bioprinted intestinal stromal cells support the growth of the epithelial monolayer to obtain a functional 3D in vitro model of the small intestinal mucosa

Once demonstrated the suitability of the bioprinted 3D hydrogels for cell culture, we combined the cell-laden GelMA-PEGDA bioprints with the co-culture of epithelial cells on top to create a 3D *in vitro* model of the small intestinal mucosa. Fibroblast-laden hydrogels including villus and crypt features were bioprinted by mixing the GelMA-PEGDA bioink with

NIH-3 T3 cells at a density of 7.5·10^6 cells/mL. After the bioprinting process, samples were mounted in Transwell® inserts and Caco-2 cells were seeded on top (Fig. 5A).

After 21 days in culture, Caco-2 cells fully covered the fibroblast-laden hydrogels by a continuous epithelial monolayer (Fig. 5B right). The embedded fibroblasts were key for the development of the epithelial monolayer, since Caco-2 cells grown on top of cell-free hydrogels used as controls did not achieve a fully covered monolayer; colonizing the villus tips but being clustered on the crypts' and base regions creating some uncovered areas (Fig. 5B left). The epithelial surface coverage can be better observed with the histological cuts (Fig. 5C). Samples with only epithelium growing onto a cell-free hydrogel showed discontinuities in the epithelial monolayer, mainly at the crypt regions (Fig. 5C top), which may be attributed to the lower adhesion forces between cells and the concave substrate due to the soft nature of the gels [13,61]. In contrast, the model of the full mucosa with the stromal and epithelial compartments showed a continuous monolayer supported by an underneath lining of embedded fibroblasts (Fig. 5C bottom). In both cases, epithelial cells grown on top of both fibroblast-laden and control the bioprinted hydrogels showed accumulation of F-actin at their apical region, which is compatible with the presence of brush borders skeleton of polarized intestinal epithelia.

We also assessed the effective barrier function of the epithelial monolayers by measuring the transepithelial electrical resistance (TEER) along the culture time (Fig. 5D). Consistent with the microscopy observations, control samples showed very low TEER values, corresponding to uncomplete epithelial monolayers. In contrast, TEER values of fibroblast-laden hydrogels with Caco-2 cells on top experienced a boost after 9–11 days in co-culture and increase until forming a plateau from day 15 on, reaching values of ~200 $\Omega\,cm^2$. These values are similar to those reported for Caco-2 epithelial monolayers grown on 3D villous structures [6,62]. Therefore, from these experiments we can conclude that the presence of the fibroblasts favors the growth of the epithelial monolayers on top of GelMA-PEGDA bioprinted hydrogels. Previous works have also reported an increased epithelial proliferation and differentiation in co-cultures of fibroblasts and epithelial cells [13,47,49]. However, this epithelial-stromal crosstalk did not only affect the epithelial barrier development. We also observed a characteristic cell distribution of the embedded fibroblasts along the crypt-villus axis. While cell density within the hydrogel bulk and the core of the villi was quite low, fibroblasts accumulated at the tips of the villous structures and the crypt regions, regions where the surface of the sample suffer more abrupt changes (Fig. 6A). Such uneven fibroblast distribution along the crypt-villus axis has a striking resemblance to what has been previously reported in the field [8,11]. Moreover, not only fibroblast distribution but also their morphology and appear is dependent on their specific location across the sample. Fibroblasts surrounded by hydrogel showed a roundish morphology and fibroblasts closer to the epithelial layer exhibited an elongated morphology. Specifically, in the tip fibroblasts assembled in a compact multilayered manner (Fig. 6Aa), whereas in the crypts appeared less packed, but spread, forming an entangled mesh oriented towards the epithelial monolayer (Fig. 6Ab). On contrary, in the lateral surface of the villous structures, fibroblasts were elongated but sparse (Fig. 6Ac). This cell distribution would favor the attachment and growth of the epithelial Caco-2 cells. In fact, we observed a highly defined accumulation of laminin underneath the epithelial cells,
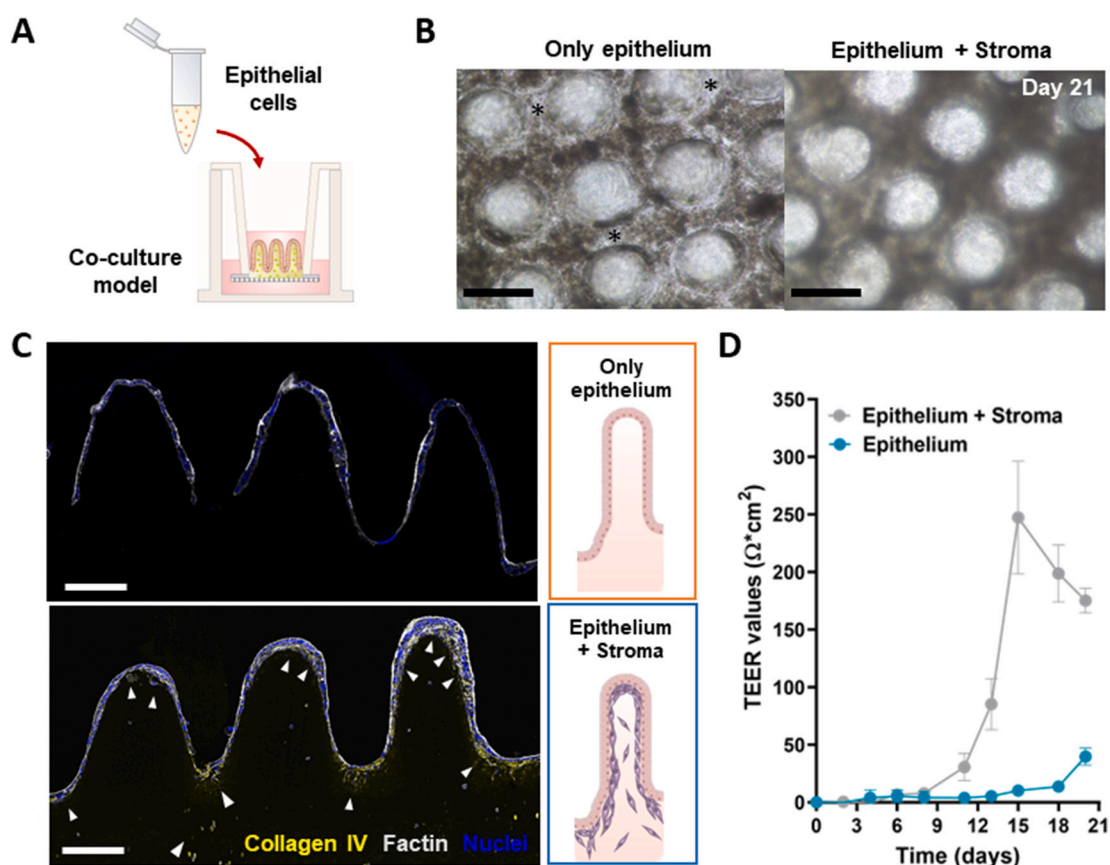
Fig. 5. Monitoring of the 3D printed intestinal mucosa model: (A) Schematic illustration of the Caco-2 seeding process on printed structures previously assembled on modified Transwell® insert. (B) Brightfield images of co-culture and control samples after 21 days in culture. * denote regions non-covered by the epithelial monolayer. Scale bars = 100 μm. (C) Mean +/− SEM, $n = 7$ (min). Immunostaining on histological cuts showing epithelial and fibroblast distribution after 21 days in culture: F-actin (grey), Collagen IV (yellow), Nuclei (blue). Scale bars = 200 μm. (D) TEER values showing the Caco-2 monolayer progression on top of the printed hydrogels with and without containing embedded NIH-3 T3.
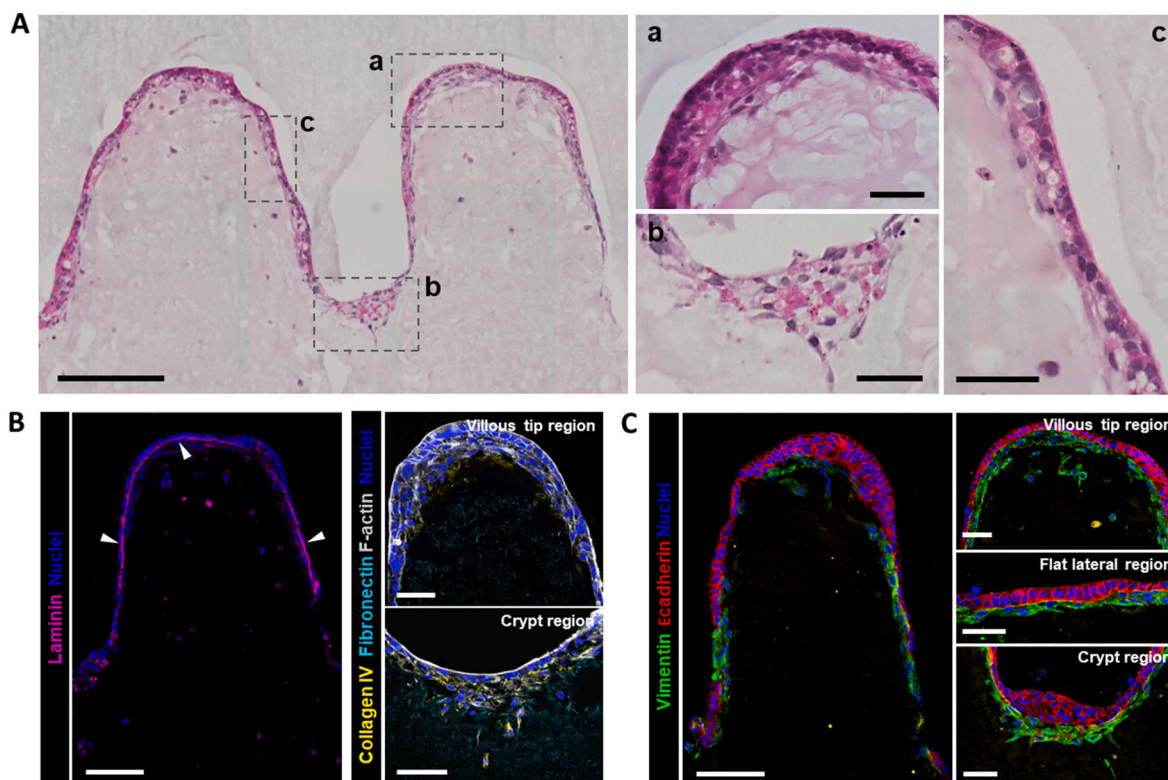
Fig. 6. Effect of the epithelium on the stromal distribution. (A) H&E staining showing fibroblasts distribution at different regions of the samples and their co-localization with epithelial cells: villus tip (a), crypt (b) and lateral villus surface (c). Scale bars = 100 μm and 20 μm details. (B-C) Immunostainings of the main markers for both cellular compartments at different regions of the microstructures. (B) Laminin (magenta), collagen IV (yellow) and fibronectin (cyan) evidence the fibroblast activity within the gels and the formation of the basement membrane. Sale bars = 100 μm and 20 μm details. (C) E-cadherin (red) and vimentin (green) show the distribution and localization of both cell types. Scale bars = 100 μm and 20 μm details. All samples were fixed and stained after 21 days of culture.

characteristic of the intestinal basement membrane (Fig. 6B), which also endows epithelium growth [63]. Collagen IV, another main component of the intestinal basement membrane, was also deposited underneath the epithelial monolayer (Fig. 5C and Fig. 6B). In this case, we observed an increased expression of collagen IV by the cells located at the crypt regions, suggesting different functionalities depending on the cell location. Other ECM proteins present in the intestinal interstitial matrix such as fibronectin were also expressed in our bioprinted 3D gut model (Fig. 6B). Thus, when in co-culture, fibroblasts showed the capability of remodeling the matrix acting as basement membrane, providing a proper cellular microenvironment for the growth and migration of the epithelial cells and promoting the maturation of their junctions as shown in the expression of the intercellular junctions E-cadherin, β-catenin and ZO-1 (Fig. 6C and Fig. S9). Epithelial morphology appeared as evolving from columnar at the crypts and the tips of the villi, to cuboidal along their walls for both samples (Fig. 6C). Concomitantly, epithelial cell density also varied along the 3D structures. These findings agree with the results found in similar 3D *in vitro* models [45], and, more importantly, with results reported from *in vivo* studies the intestinal epithelium [64,65].

4. Discussion

The use of light-based 3D printing techniques has grown exponentially in the past years, becoming one of the most promising fabrication strategies in the bioengineering field [21]. The combination of bioinks with cells to produce complex 3D functional living tissues is of particular interest [20,21]. However, the presence of living cells imposes specific requirements on the printing process to avoid cell stress and toxicity. Specifically, the nature and concentration of the photoinitiator employed, the printing time and dose, and the light source used should

be carefully controlled [21].

In this work we customized a DLP-based bioprinting system based on visible-light photopolymerization and proved its suitability for the controlled printing of cell-laden bioinks with low macromer content. The apparatus was successfully adapted for printing highly transparent photosensitive polymers in reduced volumes, including temperature sensitive materials such as GelMA, and cell-laden bioinks, leading to high cell viability rates. Despite similar systems have been previously introduced [14,66–68], it is still challenging to faithfully crosslink solutions of low macromer content (< 10 % *w/v*), which are key to guarantee the survival of cells in soft tissues [50,53]. These polymeric solutions render hydrogels that possess variable swelling and mechanical properties in the range of those featured by soft tissues (< 40 kPa) [13,68], which can be adapted on demand to better recreate the particular physicochemical properties of different extracellular matrix tissues, including cell adhesion and matrix remodeling capabilities, while having good mass transfer properties to allow cell viability for long time periods. By investigating the printing parameters suitable to produce well defined and mechanically stable printed constructs of GelMA - PEGDA polymer solutions, we could estimate the impact of the main printing parameters (printed layer thickness, printing time per layer, exposure intensity, CAD design characteristics) on the bioprinting process. It is worth to mention that these parameters are entangled in printing process and, while on the one hand make pose some difficulties to find the proper conditions, on the other hand, when using a suitable bioink, provide the system with an easy, straightforward methodology to fine tune the crosslinking density of the hydrogel. Additionally, the optical characteristics of the bioink were also adjusted by adding a photosensitive dye, tartrazine, to the prepolymer mixture [32,34]. We found that by adjusting the content of tartrazine, it is possible to modify the gelation kinetics of the bioink and achieve a better confinement of

the crosslinking reaction, thus, minimizing the undesired overexposure effects. With this approach, we can produce in a reproducible and reliable manner mechanically stable hydrogel prints of complex architectures such as the crypt-villus structures mimicking the small intestinal mucosa. We employed as bioink a mixture of a natural derived polymer (GelMA) and a synthetic polymer (PEGDA) that provide both cell adhesion and remodeling cues and mechanical long-term stability [7,13,53,69], and we obtain a functional *in vitro* 3D model of the intestinal mucosa containing the epithelial but also the stromal compartment. Multiple works have demonstrated the importance of including the 3D architecture of the small intestinal tissue when addressing questions going from basic biology till drug absorption, drug-pathogen interactions, or disease modeling [6,7,62,69,70]. However, the role of the stromal compartment in these structured 3D models has been largely neglected due to the challenge of their biofabrication. With our optimized bioprinting procedure we could successfully obtain hydrogels that not only feature the crypt-villus architecture of the native tissue, but also include the relevant cell populations of the stromal and epithelial compartments and its functionality as tissue barrier, thus providing a unique *in vitro* model of the intestinal mucosa. This model is compatible with the standard assays such as TEER measurements or histological stainings, emphasizing its potential applications in the field of *in vitro* tissue modeling. Furthermore, we could evidence the crosstalk between the different cell populations. The embedded fibroblasts boosted the growth and differentiation of the epithelial monolayer, forming a continuous effective barrier. These interactions have been mainly attributed to the paracrine signaling *via* hepatocyte growth factor (HGF) and keratinocyte growth factor (KGF), among others secreted by the mesenchymal cells [47,49]. However, we have also observed that these encapsulated fibroblasts secreted laminin and collagen IV that form a highly defined basement membrane underneath the epithelium. These ECM proteins would also contribute to the formation and differentiation of the epithelial barrier.

Noteworthy, this epithelial-mesenchymal crosstalk is bidirectional. Fibroblasts close to the surface showed a migratory phenotype towards the epithelium. Also, the histological studies revealed a characteristic distribution of the embedded fibroblasts, which accumulate at the tips of the villi and the crypt regions similar to what has been shown *in vivo* [64,65,71,72]. Interestingly, those are regions with a highly curved surface, convex or concave. In the recent years, the effect of the local curvature on cell behavior has gain a lot of attention [71–73]. Our bioprinted model would allow to study the effect of the tissue architecture and curvature not only on the epithelial cells of the surface but also on the migration, proliferation and distribution of the encapsulated cells.

Another main application of our bioprinted model of the intestinal mucosa is the impact of the 3D architecture on drug transport. We have recently demonstrated that the bioprinted villus-like topography significantly affected the expression of relevant drug transporters providing a more physiological model to study drug absorption [74]. Thus, our light-based 3D bioprinting approach paves the way to obtain physiologically relevant tissue models in a robust and systematic manner to be used in multiple fields of research. Besides, this approach does not have any inherent constraint to be scalable to the size of a conventional well-plate, thus providing a suitable alternative to include complex 3D models of tissues in standard assays.

CRediT authorship contribution statement

Conceptualization: EM, NT; methodology: NT, JZ; validation: JZ, NT, EA; investigation: NT, JZ, EA, MG, AC; Visualization: NT, MG; supervision: EM, NT; writing—original draft: NT, MG, EM.

Declaration of competing interest

The authors declare that they have no known competing financial interests or personal relationships that could have appeared to influence the work reported in this paper.

Data availability

Data will be made available on request.

Acknowledgements

Appendix A. Supplementary data

Supplementary data to this article can be found online at https://doi.org/10.1016/j.bioadv.2023.213534.

References

[1] A.C. Luca, S. Mersch, R. Deenen, S. Schmidt, I. Messner, K.-L. Schäfer, et al., Impact of the 3D microenvironment on phenotype, gene expression, and EGFR inhibition of colorectal Cancer cell lines, PLoS One 8 (2013), e59689.

[2] J.R. Turner, Intestinal mucosal barrier function in health and disease, Nat Rev Immunol 9 (2009) 799–809, https://doi.org/10.1038/nri2653.

[3] A. Abbott, Biology's new dimension, Nature 424 (2003) 870–872, doi:https://doi-org.sire.ub.edu/10.1038/424870a.

[4] K.R. Johnson, J.L. Leight, V.M. Weaver, Demystifying the effects of a three-dimensional microenvironment in tissue morphogenesis, Methods Cell Biol. 83 (2007) 547–583, https://doi.org/10.1016/S0091-679X(07)83023-8.

[5] H.J. Kim, H. Li, J.J. Collins, D.E. Ingber, Contributions of microbiome and mechanical deformation to intestinal bacterial overgrowth and inflammation in a human gut-on-a-chip, Proc. Natl. Acad. Sci. 113 (2015) 201522193, https://doi.org/10.1073/pnas.1522193112.

[6] A. García Castaño, M. García-Díaz, G. Altay, N. Torras, E. Martínez, Dynamic photopolymerization produces complex microstructures on soft hydrogels in a moldless approach to generate a 3D intestinal tissue model, Biofabrication 11 (2018) 1–15, 025007.

[7] J. Yu, S. Peng, D. Luo, J.C. March, In vitro 3D human small intestinal villous model for drug permeability determination, Biotechnol. Bioeng. 109 (2012) 2173–2178, https://doi.org/10.1002/bit.24518.

[8] D.W. Powell, I. Pinchuk, v, Saada JI, Chen X, Mifflin RC., Mesenchymal cells of the intestinal lamina propria, Annu. Rev. Physiol. 73 (2011) 213–237, https://doi.org/10.1146/annurev.physiol.70.113006.100646.

[9] M. Verhulsel, A. Simon, M. Bernheim-Dennery, V.R. Gannavarapu, L. Gérémie, D. Ferraro, et al., Developing an advanced gut on chip model enabling the study of epithelial cell/fibroblast interactions, Lab Chip 21 (2021) 365–377, https://doi.org/10.1039/D0LC00672F.

[10] V. de Gregorio, G. Imparato, F. Urciuolo, P.A. Netti, 3D stromal tissue equivalent affects intestinal epithelium morphogenesis in vitro, Biotechnol. Bioeng. 115 (2018) 1062–1075, https://doi.org/10.1002/bit.26522.

[11] M. Roulis, R.A. Flavell, Fibroblasts and myofibroblasts of the intestinal lamina propria in physiology and disease, Differentiation 92 (2016) 116–131, https://doi.org/10.1016/j.diff.2016.05.002.

[12] C.M. Costello, J. Hongpeng, S. Shaffiey, J. Yu, N.K. Jain, D. Hackam, et al., Synthetic small intestinal scaffolds for improved studies of intestinal differentiation, Biotechnol. Bioeng. 111 (2014) 1222–1232, https://doi.org/10.1002/bit.25180.

[13] A. Vila, N. Torras, A.G. Castaño, M. García-Díaz, J. Comelles, T. Pérez-Berezo, et al., Hydrogel co-networks of gelatine methacrylate and poly(ethylene glycol) diacrylate sustain 3D functional in vitro models of intestinal mucosa, Biofabrication (2020) 12, https://doi.org/10.1088/1758-5090/ab5f50.

[14] J. Creff, R. Courson, T. Mangeat, J. Foncy, S. Souleille, C. Thibault, et al., Fabrication of 3D scaffolds reproducing intestinal epithelium topography by high-resolution 3D stereolithography, Biomaterials 221 (2019), 119404, https://doi.org/10.1016/j.biomaterials.2019.119404.

[15] J.H. Sung, J. Yu, D. Luo, M.L. Shuler, J.C. March, Microscale 3-D hydrogel scaffold for biomimetic gastrointestinal (GI) tract model, Lab Chip 11 (2011) 389–392, https://doi.org/10.1039/c0lc00273a.

[16] Y. Wang, D.B. Gunasekara, M.I. Reed, M. DiSalvo, S.J. Bultman, C.E. Sims, et al., A microengineered collagen scaffold for generating a polarized crypt-villus architecture of human small intestinal epithelium, Biomaterials 128 (2017) 44–55, https://doi.org/10.1016/j.biomaterials.2017.03.005.

[17] M.H. Macedo, A.S. Barros, E. Martínez, C.C. Barrias, B. Sarmento, All layers matter: innovative three-dimensional epithelium-stroma-endothelium intestinal model for reliable permeability outcomes, J. Control. Release 341 (2022) 414–430, https://doi.org/10.1016/j.jconrel.2021.11.048.

[18] M. Nikolaev, O. Mitrofanova, N. Broguiere, S. Geraldo, D. Dutta, Y. Tabata, et al., Homeostatic mini-intestines through scaffold-guided organoid morphogenesis, Nature 585 (2020) 574–578, https://doi.org/10.1038/s41586-020-2724-8.

[19] W. Xi, J. Saleh, A. Yamada, C. Tomba, B. Mercier, S. Janel, et al., Modulation of designer biomimetic matrices for optimized differentiated intestinal epithelial cultures, Biomaterials 282 (2022), 121380, https://doi.org/10.1016/j.biomaterials.2022.121380.

[20] S. Vijayavenkataraman, W. Yan, W. Feng, C. Wang, J. Ying, H. Fuh, 3D bioprinting of tissues and organs for regenerative medicine, Adv. Drug Deliv. Rev. 132 (2018) 296–332, https://doi.org/10.1016/j.addr.2018.07.004.

[21] S. Murphy, v., Atala A., 3D bioprinting of tissues and organs, Nat. Biotechnol. 32 (2014) 773–785, https://doi.org/10.1038/nbt.2958.

[22] W. Kim, G. Kim, Intestinal villi model with blood capillaries fabricated using collagen-based bioink and dual-cell-printing process, ACS Appl. Mater. Interfaces 10 (2018) 41185–41196, https://doi.org/10.1021/acsami.8b17410.

[23] S. Kyle, Z.M. Jessop, A. Al-Sabah, I.S. Whitaker, "Printability" of candidate biomaterials for extrusion based 3D printing: state-of-the-art, Adv Healthc Mater 6 (2017), https://doi.org/10.1002/adhm.201700264, 1700264.

[24] K.S. Lim, J.H. Galarraga, X. Cui, G.C.J. Lindberg, J.A. Burdick, T.B.F. Woodfield, Fundamentals and applications of photo-cross-linking in bioprinting, Chem. Rev. 120 (2020) 10662–10694, https://doi.org/10.1021/acs.chemrev.9b00812.

[25] W. Kim, G.H. Kim, An innovative cell-printed microscale collagen model for mimicking intestinal villus epithelium, Chem. Eng. J. 334 (2018) 2308–2318, https://doi.org/10.1016/j.cej.2017.12.001.

[26] R. Levato, T. Jungst, R.G. Scheuring, T. Blunk, J. Groll, J. Malda, From shape to function: the next step in bioprinting, Adv. Mater. 32 (2020) 1906423, https://doi.org/10.1002/adma.201906423.

[27] H. Kang, S.J. Lee, I.K. Ko, C. Kengla, J.J. Yoo, A. Atala, A 3D bioprinting system to produce human-scale tissue constructs with structural integrity, Nat. Biotechnol. 34 (2016) 312–319, https://doi.org/10.1038/nbt.3413.

[28] R. Chang, J. Nam, W. Sun, Effects of dispensing pressure and nozzle diameter on cell survival from solid freeform fabrication–based direct cell writing, Tissue Eng Part A 14 (2008) 41–48, https://doi.org/10.1089/ten.a.2007.0004.

[29] P. Soman, P.H. Chung, A.P. Zhang, S. Chen, Digital microfabrication of user-defined 3D microstructures in cell-laden hydrogels, Biotechnol. Bioeng. 110 (2013) 3038–3047, https://doi.org/10.1002/bit.24957.

[30] J.R. Tumbleston, D. Shirvanyants, N. Ermoshkin, R. Janusziewicz, A.R. Johnson, D. Kelly, et al., Continuous liquid interface production of 3D objects, Science 2015 (347) (1979) 1349, https://doi.org/10.1126/science.aaa2397.

[31] W.L. Ng, J.M. Lee, M. Zhou, Y.-W. Chen, K.-X.A. Lee, W. Yeong, et al., Vat polymerization-based bioprinting—process, materials, applications and regulatory challenges, Biofabrication 12 (2020) 1–23, https://doi.org/10.1088/1758-5090/ab6034.

[32] H. Gong, B.P. Bickham, A.T. Woolley, G.P. Nordin, Custom 3D printer and resin for 18 μm × 20 μm microfluidic flow channels, Lab Chip 17 (2017) 2899–2909, https://doi.org/10.1039/C7LC00644F.

[33] Z. Wang, H. Kumar, Z. Tian, X. Jin, J.F. Holzman, F. Menard, et al., Visible light Photoinitiation of cell-adhesive gelatin Methacryloyl hydrogels for Stereolithography 3D bioprinting, ACS Appl. Mater. Interfaces 10 (2018) 26859–26869, https://doi.org/10.1021/acsami.8b06607.

[34] B. Grigoryan, S.J. Paulsen, D.C. Corbett, D.W. Sazer, C.L. Fortin, A.J. Zaita, et al., Multivascular networks and functional intravascular topologies within biocompatible hydrogels, Science 2019 (364) (1979) 458–464, https://doi.org/10.1126/science.aav9750.

[35] H. Lin, D. Zhang, P.G. Alexander, G. Yang, J. Tan, A.W.-M. Cheng, et al., Application of visible light-based projection stereolithography for live cell-scaffold fabrication with designed architecture, Biomaterials 34 (2013) 331–339, https://doi.org/10.1016/j.biomaterials.2012.09.048.

[36] Z. Wang, X. Jin, Z. Tian, F. Menard, J.F. Holzman, K. Kim, A novel, well-resolved direct laser bioprinting system for rapid cell encapsulation and microwell fabrication, Adv Healthc Mater 7 (2018) 1–11, https://doi.org/10.1002/adhm.201701249.

[37] A. Nguyen, P. Goering, V. Reipa, R. Narayan, Toxicity and photosensitizing assessment of gelatin methacryloyl-based hydrogels photoinitiated with lithium phenyl-2,4,6-trimethylbenzoylphosphinate in human primary renal proximal tubule epithelial cells, Biointerphases 14 (2019) 1–8, https://doi.org/10.1116/1.5095886.

[38] Giuseppe MDI, N. Law, B. Webb, A.R. Macrae, L.J. Liew, T.B. Sercombe, et al., Mechanical behaviour of alginate-gelatin hydrogels for 3D bioprinting, J. Mech. Behav. Biomed. Mater. 79 (2018) 150–157, https://doi.org/10.1016/j.jmbbm.2017.12.018.

[39] W. Zhu, H. Cui, B. Boualam, F. Masood, E. Flynn, R.D. Rao, et al., 3D bioprinting mesenchymal stem cell-laden construct with core-shell nanospheres for cartilage tissue engineering, Nanotechnology 29 (2018) 1–10, https://doi.org/10.1088/1361-6528/aaafa1.

[40] D. Loessner, C. Meinert, E. Kaemmerer, L.C. Martine, K. Yue, P.A. Levett, et al., Functionalization, preparation and use of cell-laden gelatin methacryloyl–based

[41] A. van den Bulcke, B. Bogdanov, N. de Rooze, E. Schacht, M. Cornelissen, H. Berghmans, Structural and rheological properties of methacrylamide modified gelatin hydrogels, Biomacromolecules 1 (2000) 31–38, https://doi.org/10.1021/bm990017d.

[42] O. Okeowo, J.R. Dorgan, Multicomponent swelling of polymer networks, Macromolecules 39 (2006) 8193–8202, https://doi.org/10.1021/ma0618124.

[43] C.J. Lee, J.A. Vroom, H.A. Fishman, S.F. Bent, Determination of human lens capsule permeability and its feasibility as a replacement for Bruch's membrane, Biomaterials 27 (2006) 1670–1678, https://doi.org/10.1016/j.biomaterials.2005.09.008.

[44] K. Engberg, C.W. Frank, Protein diffusion in photopolymerized poly(ethylene glycol) hydrogel networks, Biomed. Mater. 6 (2011) 55006, https://doi.org/10.1088/1748-6041/6/5/055006.

[45] G. Altay, S. Tosi, M. García-Díaz, E. Martínez, Imaging the cell morphological response to 3D topography and curvature in engineered intestinal tissues, Front Bioeng Biotechnol 8 (2020) 1–12, https://doi.org/10.3389/fbioe.2020.00294.

[46] M. Leulescu, A. Rotaru, I. Palarie, A. Moanta, N. Cioatera, M. Popescu, et al., Tartrazine: physical, thermal and biophysical properties of the most widely employed synthetic yellow food-colouring azo dye, J. Therm. Anal. Calorim. 134 (2018) 209–231, doi:10.1007/s10973-018-7663-3(0123456789.,-volV) (0123456789.,-volV).

[47] V. Visco, F.A. Bava, F. d'Alessandro, M. Cavallini, V. Ziparo, M.R. Torrisi, Human colon fibroblasts induce differentiation and proliferation of intestinal epithelial cells through the direct paracrine action of keratinocyte growth factor, J. Cell. Physiol. 220 (2009) 204–213, https://doi.org/10.1002/jcp.21752.

[48] R.E. Hynds, P. Bonfanti, S.M. Janes, Regenerating human epithelia with cultured stem cells: feeder cells, organoids and beyond, EMBO Mol Med 10 (2018) 139–150, https://doi.org/10.15252/emmm.201708213.

[49] M. Göke, M. Kanai, D.K. Podolsky, Intestinal fibroblasts regulate intestinal epithelial cell proliferation via hepatocyte growth factor, American Journal of Physiology-Gastrointestinal and Liver Physiology 274 (1998) G809–G818, https://doi.org/10.1152/ajpgi.1998.274.5.G809.

[50] J. Louis-Auguste, S. Greenwald, M. Simuyandi, R. Soko, R. Banda, P. Kelly, High dose multiple micronutrient supplementation improves villous morphology in environmental enteropathy without HIV enteropathy: results from a double-blind randomised placebo controlled trial in Zambian adults, BMC Gastroenterol. 14 (2014) 15, https://doi.org/10.1186/1471-230X-14-15.

[51] P. Mpountoukas, A. Pantazaki, E. Kostareli, P. Christodoulou, D. Kareli, S. Poliliou, et al., Cytogenetic evaluation and DNA interaction studies of the food colorants amaranth, erythrosine and tartrazine, Food Chem. Toxicol. 48 (2010) 2934–2944, https://doi.org/10.1016/j.fct.2010.07.030.

[52] B. Soares, T. Araújo, J. Ramos, L. Pinto, B. Khayat, Bahia M. de Oliveira, et al., Effects on DNA repair in human lymphocytes exposed to the food dye tartrazine yellow, Anticancer Res. 35 (2015) 1465–1474.

[53] M.A. Daniele, A.A. Adams, J. Naciri, S.H. North, F.S. Ligler, Interpenetrating networks based on gelatin methacrylamide and PEG formed using concurrent thiol click chemistries for hydrogel tissue engineering scaffolds, Biomaterials 35 (2014) 1845–1856, https://doi.org/10.1016/j.biomaterials.2013.11.009.

[54] M. Zhu, Y. Wang, G. Ferracci, J. Zheng, N.-J. Cho, B.H. Lee, Gelatin methacryloyl and its hydrogels with an exceptional degree of controllability and batch-to-batch consistency, Sci. Rep. 9 (2019) 6863, https://doi.org/10.1038/s41598-019-42186-x.

[55] T.R. Cox, J.T. Erler, Remodeling and homeostasis of the extracellular matrix: implications for fibrotic diseases and cancer, Dis. Model. Mech. 4 (2011) 165–178, https://doi.org/10.1242/dmm.004077.

[56] C.F. Guimarães, L. Gasperini, A.P. Marques, R.L. Reis, The stiffness of living tissues and its implications for tissue engineering, Nat Rev Mater 5 (2020) 351–370, https://doi.org/10.1038/s41578-019-0169-1.

[57] T.G. Mezger, C. Sprinz, A. Green, Applied Rheology: With Joe Flow on Rheology Road, 5th ed., Anton Paar, Graz, Austria, 2015.

[58] V. Chan, P. Zorlutuna, J.H. Jeong, H. Kong, R. Bashir, Three-dimensional photopatterning of hydrogels using stereolithography for long-term cell encapsulation, Lab Chip 10 (2010) 2062–2070, https://doi.org/10.1039/C004285D.

[59] K.R. Mamaghani, S.M. Naghib, A. Zahedi, M. Rahmanian, M. Mozafari, GelMa/PEGDA containing graphene oxide as an IPN hydrogel with superior mechanical performance, Mater Today Proc 5 (2018) 15790–15799, https://doi.org/10.1016/j.matpr.2018.04.193.

[60] K.S. Kolahi, A. Donjacour, X. Liu, W. Lin, R.K. Simbulan, E. Bloise, E.R.P. Maltepe, Effect of substrate stiffness on early mouse embryo development, PLoS One (2012) 7, https://doi.org/10.1371/journal.pone.0041717.

[61] S. Ehrig, B. Schamberger, C.M. Bidan, A. West, C. Jacobi, K. Lam, et al., Surface tension determines tissue shape and growth kinetics, Sci. Adv. 5 (2023) eaav9394, https://doi.org/10.1126/sciadv.aav9394.

[62] M. García-Díaz, M.D. Cendra, R. Alonso-Roman, M. Urdániz, E. Torrents, E. Martínez, Mimicking the intestinal host-pathogen interactions in a 3D in vitro model: the role of the mucus layer, Pharmaceutics (2022) 14, https://doi.org/10.3390/pharmaceutics14081552.

[63] D. Vllasaliu, F.H. Falcone, S. Stolnik, M. Garnett, Basement membrane influences intestinal epithelial cell growth and presents a barrier to the movement of macromolecules, Exp. Cell Res. 323 (2014) 218–231, https://doi.org/10.1016/j.yexcr.2014.02.022.

[64] D. Krndija, F. el Marjou, B. Guirao, S. Richon, O. Leroy, Y. Bellaiche, et al., Active cell migration is critical for steady-state epithelial turnover in the gut, Science 365 (2019) 705–710, https://doi.org/10.1126/science.aau3429.

[65] P. Rowart, P. Erpicum, J.-M. Krzesinski, M. Sebbagh, F. Jouret, Mesenchymal stromal cells accelerate epithelial tight junction assembly via the AMP-activated protein kinase pathway, independently of liver kinase B1, Stem Cells Int. 2017 (2017) 9717353, https://doi.org/10.1155/2017/9717353.

[66] B. Srinivasan, A.R. Kolly, M.B. Esch, H.E. Abaci, M.L. Shuler, TEER measurement techniques for in vitro barrier model systems, J Lab Autom 20 (2015) 107–126, https://doi.org/10.1177/2211068214561025.

[67] N. Taebnia, R. Zhang, E.B. Kromann, A. Dolatshahi-Pirouz, T.L. Andresen, N. B. Larsen, Dual-material 3D-printed intestinal model devices with integrated villi-like scaffolds, ACS Appl. Mater. Interfaces 13 (2021) 58434–58446, https://doi.org/10.1021/acsami.1c22185.

[68] A. Bhusal, E. Dogan, H.-A. Nguyen, O. Labutina, D. Nieto, A. Khademhosseini, et al., Multi-material digital light processing bioprinting of hydrogel-based microfluidic chips, Biofabrication 14 (2021) 1–13, https://doi.org/10.1088/1758-5090/ac2d78.

[69] C.M. Costello, R.M. Sorna, Y. Goh, I. Cengic, N.K. Jain, J.C. March, 3D intestinal scaffolds for evaluating the therapeutic potential of probiotics, Mol. Pharm. 11 (2014) 2030–2039, https://doi.org/10.1021/mp5001422.

[70] F. Yanagawa, S. Sugiura, T. Kanamori, Hydrogel microfabrication technology toward three dimensional tissue engineering, Regen Ther 3 (2016) 45–57, https://doi.org/10.1016/j.reth.2016.02.007.

[71] S.J.P. Callens, R.J.C. Uyttendaele, L.E. Fratila-Apachitei, A.A. Zadpoor, Substrate curvature as a cue to guide spatiotemporal cell and tissue organization, Biomaterials 232 (2020), 119739, https://doi.org/10.1016/j.biomaterials.2019.119739.

[72] M. Werner, A. Petersen, N.A. Kurniawan, C.V.C. Bouten, Cell-perceived substrate curvature dynamically coordinates the direction, speed, and persistence of stromal cell migration, Adv Biosyst 3 (2019) 1900080, https://doi.org/10.1002/adbi.201900080.

[73] L. Pieuchot, J. Marteau, A. Guignandon, T. dos Santos, I. Brigaud, P.-F. Chauvy, et al., Curvotaxis directs cell migration through cell-scale curvature landscapes, Nat. Commun. 9 (2018) 3995, https://doi.org/10.1038/s41467-018-06494-6.

[74] Macedo MH, Torras N, García-Díaz, M, Barrias CC, Sarmento B, Martínez E. The shape of our gut: dissecting its impact on drug absorption in a 3D bioprinted intestinal model. Biomaterial Advances, (currently under review, ref. BIOADV-D-23-00057).